Proceedings of The 2021 IEEE International
Conference on Real-time Computing and Robotics
July 15-19, 2021, Xining, China

Dynamic Surface Control for an Underactuated Underwater Biomimetic Vehicle-Manipulator System

Xuejian Bai[1,2], Yu Wang[2], Rui Wang[2], Shuo Wang[1,2,3] and Min Tan[2]

Abstract— **In this paper, a position control method based on an improved dynamic surface control is proposed for an underactuated underwater biomimetic vehicle-manipulator system (UBVMS) driven by undulatory fin propulsors. A surge force adaptive process is designed to solve the underactuated problem of the UBVMS. And the proposed closed-loop control system is verified to be stable in terms of Lyapunov theory. Simulation results indicate that the proposed control method has good control effectiveness. Finally, experiments in an indoor experiment pool are implemented to validate the control method's feasibility and robustness in the applications of UBVMSs.**

I. INTRODUCTION

With the rapid development of exploitation and utilization of ocean resources, underwater vehicle-manipulator systems (UVMSs) have captured researchers' attention and are gradually being widely used [1]. The main fields of current research on the UVMSs include mechanism design, sensor and communication systems, underwater localization, autonomous control strategies, etc [2].

In the past few years, lots of research teams around the world are committed to the exploration of the UVMSs. In the United Kingdom, researchers in Heriot-watt university started a project named ALIVE to develop an UVMS capable of docking to a subsea structure. The developed UVMS can perceive the underwater environment through sonar and video sensor processing techniques and used a six-degree-of-freedom (DOF) underwater manipulator to complete fixed-point underwater tasks [3]. In 2015, Doc Ricketts, an UVMS developed by the Monterey Bay Aquarium Research Institute explored the Palos Verdes Fault offshore in Southern California [4]. The UVMS made it possible to present tectonic geomorphology and seascape evolution. The TRIDENT was an UVMS project in Europe focusing on the autonomous operation of UVMSs [5]. Based on the developed Girona-500 UVMS, this project has completed several autonomous tasks, including autonomously searching and recovering a black-box, autonomous valve turning, etc [6], [7]. In China, the manned deep submersible JIAOLONG was developed to achieved manned deep-sea diving [8]. In 2020, China's new manned deep submersible FENDOUZHE reached a depth of 10,909 meters in the Mariana Trench.

The UVMSs in the above researches are mainly driven by traditional thrusters. Recently, with the advancement of the bionic mechanism, the UVMSs driven by bionic propulsion methods have also been in progress. In Norway, a modular and flexible underwater robot capable of swimming like a snake named Eelume was developed to provide immediate response to unpredicted inspection, maintenance and repair requirements at the bottom of the sea [9]. Inspired by cuttlefish's swimming mode, RobCutt II, an underwater biomimetic vehicle-manipulator system (UBVMS) driven by undulatory fins was developed in 2018 [10]. On the basis of the developed UBVMS, underwater autonomous free floating manipulation experiments about opening a door and grasping objects were conducted [11].

The research in the control field has always been one of the research hotspots of UVMSs. Tang et al. designed a vehicle-manipulator coordinated plan and control methodology, and the autonomous grasping manipulation experiments verified the effectiveness of the proposed control methodology [12]. Cai et al. presented a depth control for an UVMS, which was implemented by an adaptive sliding mode control method, and the simulations conducted on UWSim verified the proposed control method [13]. Ma et al. presented a position control for an UBVMS by reinforcement learning method, and simulations in 5 cases verified the validity of the proposed control method [14]. Nevertheless, specialized control designs for underactuated UBVMSs are relatively rarely involved and are mainly based on simulations. Hence, this paper presented an improved dynamic surface control (DSC) method to solve the position control for an underactuated UBVMS.

In the rest of this paper, Section II presents the configuration and dynamics of the UBVMS. In Section III, the position control framework based on an improved DSC method is proposed. In Section IV, simulations and indoor experiments are implemented to verify the effectiveness of the proposed method. Finally, conclusions are summarized in Section V.

*This work was supported in part by the National Key Research and Development Program of China under Grant 2020YFC1512202, in part by the Youth Innovation Promotion Association CAS under Grant 2018162, in part by the National Natural Science Foundation of China under Grant U1713222, Grant 62073316, Grant U1806204, 62033013, in part by the Key Projects of Foreign Cooperation of CAS under Grant 173211KYSB20200020, and in part by the Strategic Priority Research Program of Chinese Academy of Science under Grant XDB32050100.

[1]School of Artificial Intelligence, University of Chinese Academy of Sciences, Beijing 100049, P. R. China

[2]Institute of Automation, Chinese Academy of Sciences, Beijing 100190, P. R. China

[3]CAS Center for Excellence in Brain Science and Intelligence Technology, Shanghai 200031, P. R. China

Corresponding author: Yu Wang, yu.wang@ia.ac.cn.

2021 IEEE International Conference on Real-time Computing and Robotics (RCAR) | 978-1-6654-3678-6/21/$31.00 ©2021 IEEE | DOI: 10.1109/RCAR52367.2021.9517609

II. CONFIGURATION AND DYNAMICS OF THE UBVMS

A. Configuration Overview of the UBVMS

As shown in Fig. 1, the UBVMS is composed of a control cabin, a visual system cabin, two symmetrically arranged biomimetic undulatory fin propulsors and a 5-DOF underwater manipulator. The mainly structure parameters of the UBVMS prototype are listed in Table I.

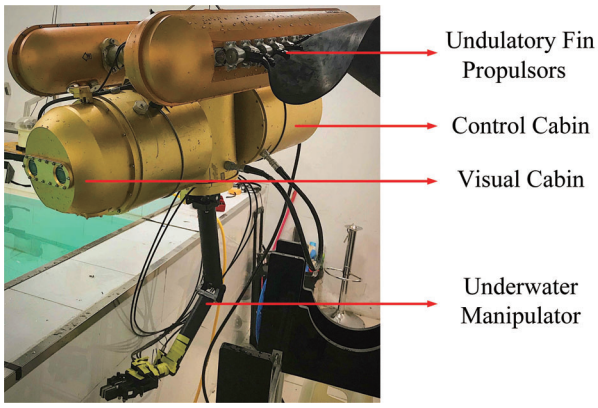

Fig. 1. Prototype of the UBVMS.

TABLE I
STRUCTURE PARAMETERS OF THE UBVMS PROTOTYPE

Parameters	Values	Parameters	Values
Mass	120.6 kg	Length	1200 mm
Width	1210 mm	Height	950 mm
Manipulator total length	1220 mm	Manipulator mass	19.4 kg
Fin width	220 mm	Fin length	550 mm
Number of fin rays	12	Fin thickness	4 mm

B. Mathematical Model of the UBVMS

In this paper, 3-DOF kinematics and dynamics are considered in the mathematical model of the UBVMS. The 3-DOF velocity vector relative to the earth-fixed frame is given by a velocity transformation:

$$\dot{\boldsymbol{\eta}} = \boldsymbol{J}(\boldsymbol{\eta})\,\boldsymbol{\nu} \tag{1}$$

where $\boldsymbol{\nu}=\begin{bmatrix} u & v & r \end{bmatrix}^{\mathrm{T}}$ denotes the velocity vector relative to the vehicle-fixed frame. $\boldsymbol{\eta} = \begin{bmatrix} x & y & \psi \end{bmatrix}^{\mathrm{T}}$ denotes the pose vector relative to the earth-fixed frame. The transformation matrix is defined as:

$$\boldsymbol{J}(\boldsymbol{\eta}) = \begin{bmatrix} \cos\psi & -\sin\psi & 0 \\ \sin\psi & \cos\psi & 0 \\ 0 & 0 & 1 \end{bmatrix} \tag{2}$$

According to Newton-Euler dynamics, the dynamic equation of the UBVMS can be written as:

$$\boldsymbol{M}_{RB}\dot{\boldsymbol{\nu}} + \boldsymbol{C}_{RB}(\boldsymbol{\nu})\,\boldsymbol{\nu} + \boldsymbol{\tau}_h(\boldsymbol{\nu}, \dot{\boldsymbol{\nu}}) = \boldsymbol{\tau} \tag{3}$$

where $\boldsymbol{M}_{RB}$ denotes the rigid-body inertia matrix, $\boldsymbol{C}_{RB}(\boldsymbol{\nu})$ denotes the rigid-body Coriolis and centripetal matrix, $\boldsymbol{\tau}=\begin{bmatrix} X & Y & N \end{bmatrix}^{\mathrm{T}}$ denotes the resultant vector of control input forces and moments, and $\boldsymbol{\tau}_h(\boldsymbol{\nu}, \dot{\boldsymbol{\nu}})$ denotes the the resultant vector of hydrodynamic force, which can be obtained in literature [14].

The detailed descriptions of $\boldsymbol{M}_{RB}$ and $\boldsymbol{C}_{RB}(\boldsymbol{\nu})$ are as follows:

$$\boldsymbol{M}_{RB} = \begin{bmatrix} m & 0 & -my_G \\ 0 & m & mx_G \\ -my_G & mx_G & I_z \end{bmatrix} \tag{4}$$

$$\boldsymbol{C}_{RB} = \begin{bmatrix} 0 & 0 & -m(x_G r + v) \\ 0 & 0 & -m(y_G r - u) \\ m(x_G r + v) & m(y_G r - u) & 0 \\ n & & \end{bmatrix} \tag{5}$$

where $m = 120.6kg$ denotes the mass of the UBVMS, $x_G = 0.015m$, $y_G = 0.008m$ represent the barycentric coordinates relative to the vehicle-fixed frame, $I_z = 15.44kg{\cdot}m^2$ denotes the moment of inertia of the UBVMS on the horizontal plane.

The UBVMS is actuated by two symmetrically arranged undulatory fin propulsors. Each undulatory fin propulsor consist of 12 fin rays and a black silicone sheet. The undulatory fin propulsors can provide the UBVMS with thrust by controlling the 12 fin rays to make the fin surface generate undulating motion. The undulating motion of each fin ray can be described as:

$$\beta_i = \beta_m \sin\left[2\pi\left(ft + x_i/\lambda\right) + \phi_0\right] + \beta_B, i = 1, 2, \cdots, 12 \tag{6}$$

where β_m denotes maximum angular deflection of the sinusoidal waves, f denotes oscillating frequency, t denotes time, λ denotes the wave length, ϕ_0 denotes the initial phase, β_i and x_i represent the deflection angle and the position of the ith fin ray, respectively; and β_B denotes the deflection angle of the undulatory fin propulsor.

The undulatory fin propulsor can generate force and moment of varying magnitude by changing the motion parameters in (6). A measurement platform is constructed to obtain the thrust-parameters relationship of the undulatory fin propulsor [15]. These experiments indicated that when $\beta_m = \pi/6$, $\lambda = 275mm$ and $\phi_0 = \beta_B = 0$, the undulatory fin propulsors can generate surge force ($X \in [-13,\ 13]$ N) and yaw moment ($N \in [-6.4,\ 6.4]$ N $\cdot$ m) with the oscillating frequency varying within $f \in [-1.7,\ 1.7]$ Hz. The relationship between the force/moment (X/N) and the two oscillating frequencies of the left and right undulatory fin propulsors (f_L, f_R) was mapping by fuzzy approach. The detailed implementation can be found in literature [16].

Considering that the UBVMS is an underactuated system and can only produced the surge force X and yaw moment N, while the sway force Y cannot be generated by the biomimetic undulatory fin propulsors, we designed a surge force adaptive processor (SFAP) to solve the problem of the underactuated UBVMS. The SFAP can be described as:

$$\begin{aligned} X = {} & \varepsilon(\Delta r_0 - \Delta r) \cdot X + \varepsilon(\Delta\psi_0 - \Delta\psi) \cdot X \\ & - \varepsilon(\Delta r_0 - \Delta r) \cdot \varepsilon(\Delta\psi_0 - \Delta\psi) \cdot X \end{aligned} \tag{7}$$

where X denotes the surge force X derived from the controller, $\varepsilon(\cdot)$ denotes the step function, Δr denotes the

distant between the actual position and the target position, $\Delta\psi$ denotes the absolute value of the difference between the actual yaw angle and target yaw angle, Δr_0 and $\Delta\psi_0$ represent the adjustment parameters.

The step function is defined as:

$$\varepsilon(t) = \begin{cases} 0, & t < 0 \\ 1, & t \geq 0 \end{cases} \tag{8}$$

III. POSITION CONTROL METHOD OF THE UBVMS BASED ON DSC

In this section, a DSC algorithm for position control of the UBVMS is presented, which introduces a low pass filter into the conventional backstepping control to avoided the "explosion of complexity" problem. The block diagram of the position control framework is shown in Fig. 2.

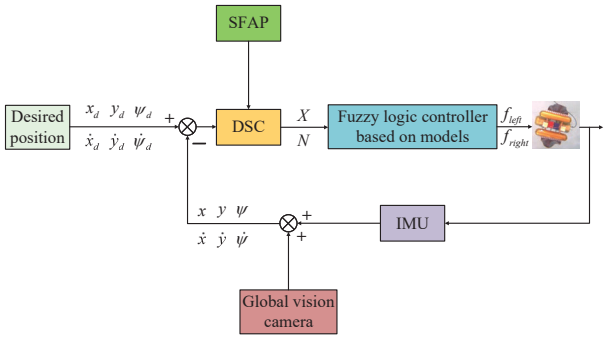

Fig. 2. Block diagram of the position control framework.

A. Dynamic Surface Control Framework Design

Transform (3) and we have:

$$\boldsymbol{M}\dot{\boldsymbol{\nu}} + \boldsymbol{C}_{RB}(\boldsymbol{\nu})\boldsymbol{\nu} + \boldsymbol{\tau}'_h(\boldsymbol{\nu})\boldsymbol{\nu} = \boldsymbol{\tau} \tag{9}$$

where $\boldsymbol{M} = \boldsymbol{M}_{RB} + \boldsymbol{M}_A$ denotes the inertia matrix including the rigid-body inertia matrix $\boldsymbol{M}_{RB}$ and the added inertia matrix $\boldsymbol{M}_A$, $\boldsymbol{\tau}'_h(\boldsymbol{\nu})\boldsymbol{\nu} = \boldsymbol{\tau}_h(\boldsymbol{\nu}, \dot{\boldsymbol{\nu}}) - \boldsymbol{M}_A\dot{\boldsymbol{\nu}}$ denotes the hydrodynamic force that removed the added inertia effects.

Choosing: $\mathbf{x}_1 = \boldsymbol{\eta}$, $\mathbf{x}_2 = \boldsymbol{\nu}$, according to (1) and (9), the dynamics are described as:

$$\begin{cases} \dot{\mathbf{x}}_1 = \boldsymbol{J}(\boldsymbol{\eta})\mathbf{x}_2 \\ \dot{\mathbf{x}}_2 = -\boldsymbol{M}^{-1}\boldsymbol{C}_{RB}(\boldsymbol{\nu})\mathbf{x}_2 - \boldsymbol{M}^{-1}\boldsymbol{\tau}'_h(\boldsymbol{\nu})\mathbf{x}_2 + \boldsymbol{M}^{-1}\boldsymbol{\tau} \end{cases} \tag{10}$$

Step 1:

Define the first error surface as

$$\mathbf{z}_1 = \mathbf{x}_1 - \boldsymbol{\eta}_d \tag{11}$$

where $\boldsymbol{\eta}_d$ denotes the desired position.

Then we have

$$\dot{\mathbf{z}}_1 = \dot{\mathbf{x}}_1 - \dot{\boldsymbol{\eta}}_d = \boldsymbol{J}(\boldsymbol{\eta})\mathbf{x}_2 - \dot{\boldsymbol{\eta}}_d \tag{12}$$

Define the second error surface as

$$\mathbf{z}_2 = \mathbf{x}_2 - \mathbf{a}_2 \tag{13}$$

where $\mathbf{a}_2$ represents a state variable.

By defining a low pass filter, we can obtain $\mathbf{a}_2$ and avoid the "explosion of complexity" problem.

$$\dot{\mathbf{a}}_2 = (\mathbf{r}_2 - \mathbf{a}_2)/e_2 \tag{14}$$

where e_2 denotes the time constant of the low pass filter, and $\mathbf{r}_2$ denotes the virtual control and is chose as

$$\mathbf{r}_2 = -\mathbf{k}_1\mathbf{z}_1 + \boldsymbol{J}(\boldsymbol{\eta})^{-1}\dot{\boldsymbol{\eta}}_d \tag{15}$$

where $\mathbf{k}_1 > 2$ denotes a designed parameter.

Step 2:

According to (10) and (13), take the derivative of $\mathbf{z}_2$ and yield:

$$\dot{\mathbf{z}}_2 = -\boldsymbol{M}^{-1}\boldsymbol{C}_{RB}(\boldsymbol{\nu})\mathbf{x}_2 - \boldsymbol{M}^{-1}\boldsymbol{\tau}'_h(\boldsymbol{\nu})\mathbf{x}_2 + \boldsymbol{M}^{-1}\boldsymbol{\tau} - \dot{\mathbf{a}}_2 \tag{16}$$

Let

$$\dot{\mathbf{z}}_2 = -\boldsymbol{J}(\boldsymbol{\eta})\mathbf{k}_2\mathbf{z}_2 \tag{17}$$

where $\mathbf{k}_2 > \frac{1}{4}$ denotes a designed parameter.

Then we have the control law as:

$$\boldsymbol{\tau} = \boldsymbol{C}_{RB}(\boldsymbol{\nu})\mathbf{x}_2 + \boldsymbol{\tau}'_h(\boldsymbol{\nu})\mathbf{x}_2 + \boldsymbol{M}(\dot{\mathbf{a}}_2 - \boldsymbol{J}(\boldsymbol{\eta})\mathbf{k}_2\mathbf{z}_2) \tag{18}$$

B. Stability Analysis

Step 1:

Define the filter error as

$$\mathbf{p}_2 = \mathbf{a}_2 - \mathbf{r}_2 \tag{19}$$

The Lyapunov function candidate is chosen as:

$$V_1 = \frac{1}{2}\mathbf{z}_1^{\mathrm{T}}\mathbf{z}_1 + \frac{1}{2}\mathbf{p}_2^{\mathrm{T}}\mathbf{p}_2 \tag{20}$$

Differentiate V_1 and combine (12), (13) and (19), we can obtain the following equation:

$$\begin{aligned} \dot{V}_1 &= \mathbf{z}_1^{\mathrm{T}}\dot{\mathbf{z}}_1 + \mathbf{p}_2^{\mathrm{T}}\dot{\mathbf{p}}_2 \\ &= \mathbf{z}_1^{\mathrm{T}}[\boldsymbol{J}(\boldsymbol{\eta})\mathbf{x}_2 - \dot{\boldsymbol{\eta}}_d] + \mathbf{p}_2^{\mathrm{T}}\dot{\mathbf{p}}_2 \\ &= \mathbf{z}_1^{\mathrm{T}}[\boldsymbol{J}(\boldsymbol{\eta})(\mathbf{z}_2 + \mathbf{a}_2) - \dot{\boldsymbol{\eta}}_d] + \mathbf{p}_2^{\mathrm{T}}\dot{\mathbf{p}}_2 \\ &= \mathbf{z}_1^{\mathrm{T}}[\boldsymbol{J}(\boldsymbol{\eta})(\mathbf{z}_2 + \mathbf{p}_2 + \mathbf{r}_2) - \dot{\boldsymbol{\eta}}_d] + \mathbf{p}_2^{\mathrm{T}}\dot{\mathbf{p}}_2 \end{aligned} \tag{21}$$

Substituting (15) into (21) yields that

$$\begin{aligned} \dot{V}_1 &= \boldsymbol{J}(\boldsymbol{\eta})\left(\mathbf{z}_1^{\mathrm{T}}\mathbf{z}_2 + \mathbf{z}_1^{\mathrm{T}}\mathbf{p}_2 - \mathbf{k}_1\|\mathbf{z}_1\|^2\right) + \mathbf{p}_2^{\mathrm{T}}\dot{\mathbf{p}}_2 \\ &\leq \boldsymbol{J}(\boldsymbol{\eta})\left(2\|\mathbf{z}_1\|^2 + \frac{1}{4}\|\mathbf{z}_2\|^2 + \frac{1}{4}\|\mathbf{p}_2\|^2 - \mathbf{k}_1\|\mathbf{z}_1\|^2\right) \\ &\quad + \mathbf{p}_2^{\mathrm{T}}\dot{\mathbf{p}}_2 \end{aligned} \tag{22}$$

Choose $\mathbf{k}_1 = 2 + a_0$ and we have

$$\dot{V}_1 \leq \boldsymbol{J}(\boldsymbol{\eta})\left(\frac{1}{4}\|\mathbf{z}_2\|^2 + \frac{1}{4}\|\mathbf{p}_2\|^2 - a_0\|\mathbf{z}_1\|^2\right) + \mathbf{p}_2^{\mathrm{T}}\dot{\mathbf{p}}_2 \tag{23}$$

According to (14), (15) and (19), we have

$$\begin{aligned} \dot{\mathbf{p}}_2 &= \dot{\mathbf{a}}_2 - \dot{\mathbf{r}}_2 \\ &= -\frac{\mathbf{p}_2}{e_2} + B_2(\mathbf{z}_1, \mathbf{z}_2, \mathbf{p}_2, \boldsymbol{\eta}_d, \dot{\boldsymbol{\eta}}_d, \ddot{\boldsymbol{\eta}}_d) \end{aligned} \tag{24}$$

where $B_2(\cdot)$ represents a continuous function and B_2 has a maximum M_2.

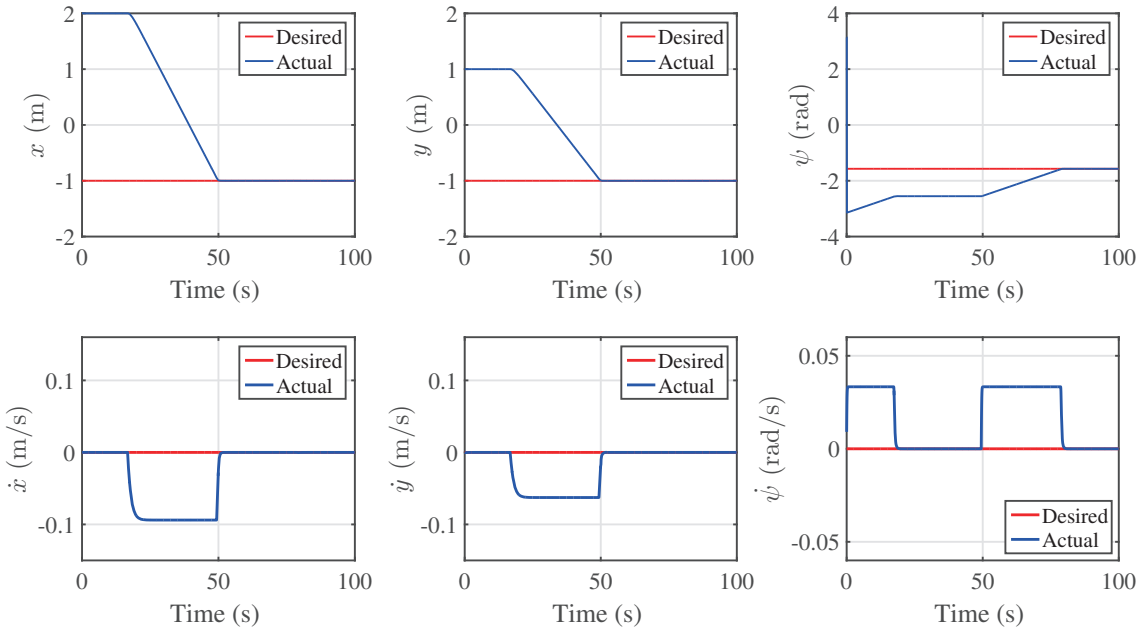

Fig. 3. Pose and velocity of the UBVMS during the position control simulation.

Choose $\frac{1}{e_2} \geq \left(\frac{1}{4}+a_0\right)\boldsymbol{J}(\boldsymbol{\eta}) + \frac{\|M_2\|^2}{2b}$ and according to Young's inequality, we can obtain that

$$\dot{V}_1 \leq M_3\left(\frac{1}{4}\|\mathbf{z}_2\|^2 - a_0\|\mathbf{z}_1\|^2 - a_0\|\mathbf{p}_2\|^2\right) + \frac{b}{2} \tag{25}$$

where M_3 denotes the maximum value of $\boldsymbol{J}(\boldsymbol{\eta})$, $a_0 > 0$ and $b > 0$ represent designed parameters.

Step 2:

Choose the Lyapunov function candidate as:

$$V_2 = V_1 + \frac{1}{2}\mathbf{z}_2^{\mathrm{T}}\mathbf{z}_2 \tag{26}$$

Then we have

$$\begin{aligned}\dot{V}_2 &= \dot{V}_1 + \mathbf{z}_2^{\mathrm{T}}\dot{\mathbf{z}}_2 \\ &\leq M_3\left(\frac{1}{4}\|\mathbf{z}_2\|^2 - a_0\|\mathbf{z}_1\|^2 - a_0\|\mathbf{p}_2\|^2 - \mathbf{k}_2\|\mathbf{z}_2\|^2\right) + \frac{b}{2}\end{aligned} \tag{27}$$

Let $\mathbf{k}_2 = \frac{1}{4} + a_0$ and we have

$$\dot{V}_2 \leq M_3\left(-a_0\|\mathbf{z}_1\|^2 - a_0\|\mathbf{p}_2\|^2 - a_0\|\mathbf{z}_2\|^2\right) + \frac{b}{2} \tag{28}$$

Finally, we can obtain that

$$\dot{V}_2 \leq -2M_3a_0V_2 + \frac{b}{2} \tag{29}$$

Then we can derive that

$$V_2(t) \leq \frac{b}{\frac{2}{t-t_0} + 4M_3a_0} + \frac{1}{1+2M_3a_0(t-t_0)}V_2(t_0) \tag{30}$$

From (30), it is observed that when $t \to \infty$, V_2 converges to $\frac{b}{4M_3a_0}$. So, the proposed control system is semiglobally uniformly bounded. And by choosing appropriate designed parameters, the tracking error converges asymptotically to a small value.

IV. SIMULATIONS AND EXPERIMENTS

In order to verify the effectiveness of the proposed control strategy, simulations and experiments are conducted to the UBVMS. The designed parameters are set as $\mathbf{k}_1 = diag(3, 0, 4.5)$, $\mathbf{k}_2 = diag(5, 0, 3)$, $e_2 = 0.1$.

A. Simulations and Analysis

The starting position and yaw angle of the UBVMS are $(2, 1)$ and π, respectively. The desired position and yaw angle of the UBVMS are $(-1, -1)$ and $-\pi/2$, respectively.

Fig. 3 shows the pose and velocity change curves of the UBVMS. The red and blue curves represent the desired and actual data of the UBVMS, respectively. It can be observed that under the action of the controller, from 0 to 18 seconds, the UBVMS first adjusts the yaw angle so that its head faces the desired position. Then from 19 to 51 seconds, the UBVMS performs the position control and reaches the desired position. Finally, from 52 to 80 seconds, the UBVMS completes the yaw control and reaches the desired yaw angle.

Fig. 4 displays the control law during the simulation. The red, blue and green curves represent the surge force X, the sway force Y and the yaw moment N, respectively. As mentioned before, the UBVMS is an underactuated system, hence the sway force of Y of the control law remains to zero. However, through the designed SFAP, the position control of the UBVMS in the y direction can be achieved. Fig. 5

demonstrates the control frequency of the fins during the simulation. The red and blue curves represent the frequency of the left fin and the right fin, respectively. Consistent with the control process, from 0 to 18 seconds, the frequency difference of the left fin and right fin provides yaw moment N to control the yaw angle. Then from 19 to 51 seconds, the fins have the same frequency with positive value to generate surge force X so that the UBVMS can swim forward in a straight line. And from 52 to 80 seconds, the yaw moment N is produced by the frequency difference to drive the UBVMS to complete control.

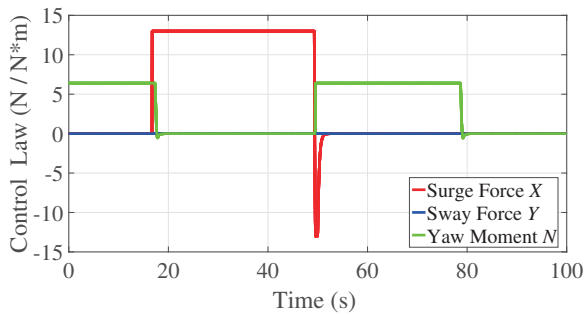

Fig. 4. Control law during the position control simulation.

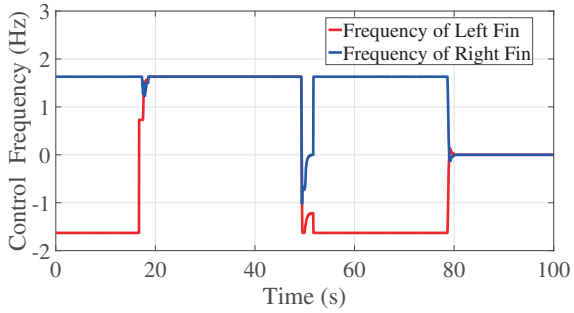

Fig. 5. Control frequency of the fins during the position control simulation.

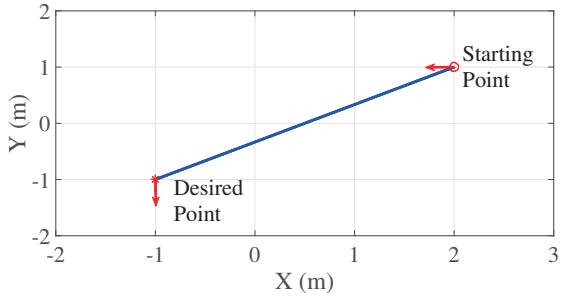

Fig. 6. Trajectory of the UBVMS during the position control simulation.

Fig. 6 displays the trajectory of the UBVMS during the simulation. The red circle and the red asterisk represent the starting point and the desired point, respectively. The red arrow and the blue curve represent the yaw angle and trajectory of the UBVMS, respectively. It can be observed from Fig. 6 that the UBVMS's trajectory is smooth and the final pose and velocity of the UBVMS reach the desired values, which indicates that the proposed control method has good control effectiveness.

B. Experiments and Results

Experiments are carried out in an indoor experiment pool. The starting position and yaw angle of the UBVMS are $(1, 1)$ and 0, respectively. The desired position and yaw angle of the UBVMS are $(-1, 0)$ and $\pi/2$, respectively.

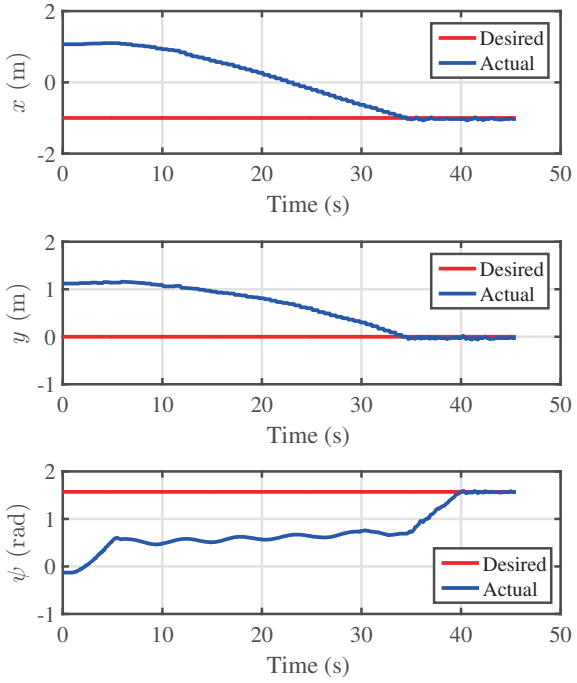

Fig. 7. Pose of the UBVMS during the position control experiment.

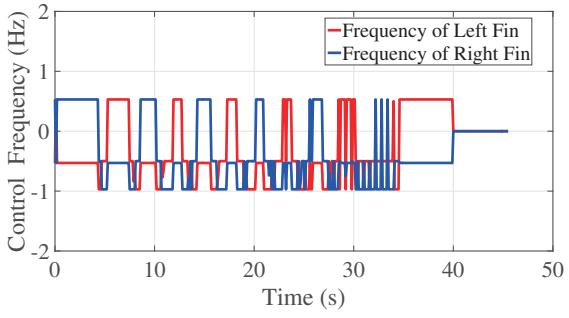

Fig. 8. Control frequency of the fins during the position control experiment.

Fig. 7 shows the UBVMS's pose during the position control experiment. The red and blue curves represent the desired and actual data of the UBVMS, respectively. During the F-UVMS's position control experiment, the actual pose of the UBVMS (x,y and ψ) reaches to the desired pose at T = $45s$ based on the proposed controller.

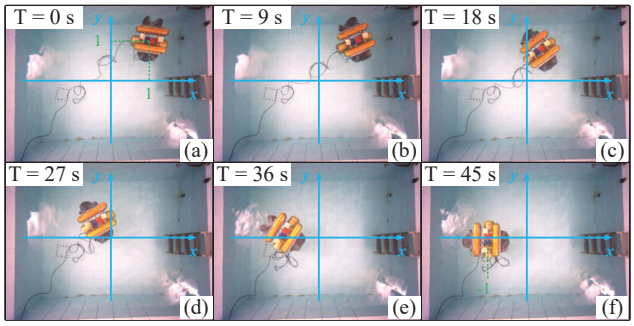

Fig. 9. Snapshots of the UBVMS during the position control experiment.

Fig. 8 displays the motion frequencies of the biomimetic undulatory fin propulsors. It is worth noting that from 9 seconds to 36 seconds, the motion frequencies of the left and right fin show oscillational changes. The disturbance of the current accounts for a significant portion of this phenomenon.

Fig. 9 shows a few images of the F-UVMS's position control experiment, where the UBVMS starts from $(1, 1)$ as shown in Fig. 9 (a) at T $= 0s$. Fig. 9 (b) to Fig. 9 (e) show the motion process of the UBVMS. In Fig. 9 (f) at T $= 45s$, the UBVMS reaches the desired pose. The experimental results show that the proposed control method exhibited good control effectiveness in the application of underwater robots.

V. CONCLUSIONS

In this paper, in order to solve the position control problem of an underactuated UBVMS, an improved DSC method combined with a surge force adaptive processor was proposed. The stability of the proposed control method was verified by the Lyapunov theory. Simulations on the UBVMS demonstrated the proposed control method can achieve accurate postion control even if the UBVMS's sway force $Y = 0$. Experimental results in an indoor experiment pool showed good control effectiveness, which validated the feasibility and robustness of the proposed control method in the application of UVMSs. In the future research, based on the proposed control method, the autonomous grasping control task of the UBVMS will be carried out.

[5] D. Ribas, et al., "I-AUV mechatronics integration for the TRIDENT FP7 Project," *IEEE/ASME Trans. Mechatronics*, vol. 20, no. 5, pp. 2583-2592, 2015.

REFERENCES

[1] H. A. Shahab, P. B. Charalampos, C. K. George, and J. K. Kostas, "Cooperative impedance control for multiple underwater vehicle manipulator systems under lean communication," *IEEE J. Ocean. Eng.*, vol. 46, no. 2, pp.447-465, 2021.

[2] A. Gianluca, Underwater Robots. Switzerland: Springer International Publishing, 2014, ch. 2.

[3] J. Evans, P. Redmond, C. Plakas, K. Hamilton, and D. Lane, "Autonomous docking for Intervention-AUVs using sonar and video-based real-time 3D pose estimation," in *OCEANS 2003*. IEEE, 2003, pp. 2201-2210.

[4] D. S. Brothers, J. E. Conrad, K. L. Maier, C. K. Paull, and M. McGann, "The Palos Verdes Fault offshore Southern California: Late Pleistocene to present tectonic geomorphology, seascape evolution, and slip rate estimate based on AUV and ROV surveys," *Journal of Geophysical Research*, vol. 120, no. 7, pp. 4734-4758, 2015.

[6] M. Prats, et al., "Multipurpose autonomous underwater intervention: a systems integration perspective," in *2012 20th Mediterranean Conference on Control and Automation*. IEEE, 2012, pp. 1379-1384.

[7] A. Carrera, N. Palomeras, N. Hurtós, P. Kormushev, and M. Carreras, "Learning multiple strategies to perform a valve turning with underwater currents using an I-AUV," in *OCEANS 2015*. IEEE, 2015, pp. 1-8.

[8] F. Liu, W.-C. Cui, and X.-Y. Li, "China's first deep manned submersible, JIAOLONG," *Science China Earth Sciences*, vol. 53, no. 10, pp. 1407-1410, 2010.

[9] P. Liljebäck, and R. Mills, "Eelume: a flexible and subsea resident IMR vehicle," in *OCEANS 2017*. IEEE, 2017, pp. 1-4.

[10] C. Tang, R. Wang, Y. Wang, S. Wang, U. F. von Lukas, and M. Tan, "RobCutt: a framework of underwater biomimetic vehicle-manipulator system for autonomous interventions," in *2018 IEEE 14th International Conference on Automation Science and Engineering*. IEEE, 2018, pp. 477-482.

[11] M.-X. Cai, S. Wang, Y. Wang, R. Wang, and M. Tan, "Coordinated control of underwater biomimetic vehicle-manipulator system for free floating autonomous manipulation," *IEEE Trans. Syst. Man Cybern.*, to be published, doi: 10.1109/TSMC.2019.2944637.

[12] C. Tang, Y. Wang, S. Wang, R. Wang, and M. Tan, "Floating autonomous manipulation of the underwater biomimetic vehicle-manipulator system: methodology and verification," *IEEE Trans. Ind. Electron.*, vol. 65, no. 6, pp. 4861-4870, 2018.

[13] M.-X. Cai, Y. Wang, S. Wang, R. Wang, and M. Tan, "ROS-based depth control for hybrid-driven underwater vehicle-manipulator system," in *2019 Chinese Control Conference*. IEEE, 2019, pp. 4576-4580.

[14] R.-C. Ma, et al., "Position control of an underwater biomimetic vehicle-manipulator system via reinforcement learning," in *2020 IEEE 9th Data Driven Control and Learning Systems Conference*. IEEE, 2020, pp. 573-578.

[15] R.-C. Ma, Y. Wang, R. Wang, and S. Wang, "Development of a propeller with undulating fins and its characteristics," in *2019 IEEE International Conference on Real-time Computing and Robotics*. IEEE, 2019, pp. 737-742.

[16] S. Wang, Y. Wang, Q. Wei, M. Tan, and J. Yu, "A bio-inspired robot with undulatory fins and its control methods," *IEEE/ASME Trans. Mechatronics*, vol. 22, no. 1, pp. 206-216, 2017.